Research article

Shasha Li, Tao Deng*, Yang Zhang, Yuning Li, Weijie Yin, Qi Chen and Zewen Liu

Solar-blind ultraviolet detection based on TiO_2 nanoparticles decorated graphene field-effect transistors

https://doi.org/10.1515/nanoph-2019-0060
Received February 26, 2019; revised April 2, 2019; accepted April 6, 2019

Abstract: Sensitive solar-blind ultraviolet (UV) photodetectors are important to various military and civilian applications, such as flame sensors, missile interception, biological analysis, and UV radiation monitoring below the ozone hole. In this paper, a solar-blind UV photodetector based on a buried-gate graphene field-effect transistor (GFET) decorated with titanium dioxide (TiO_2) nanoparticles (NPs) was demonstrated. Under the illumination of a 325-nm laser (spot size ~2 μm) with a total power of 0.35 μW, a photoresponsivity as high as 118.3 A/W was obtained, at the conditions of zero gate bias and a source-drain bias voltage of 0.2 V. This photoresponsivity is over 600 times higher than that of a recently reported solar-blind UV photodetector based on graphene/vertical Ga_2O_3 nanowire array heterojunction (0.185 A/W). Experiments showed that the photoresponsivity of the TiO_2 NPs decorated GFET photodetectors can be further enhanced by increasing the source-drain bias voltage or properly tuning the gate bias voltage. Furthermore, the photoresponse time of the TiO_2 NPs decorated GFET photodetectors can also be tuned by the source-drain bias and gate bias. This study paves a simple and feasible way to fabricate highly sensitive, cost-efficient, and integrable solar-blind UV photodetectors.

Keywords: TiO_2 nanoparticles; graphene field-effect transistor (GFET); ultraviolet (UV); photodetector.

***Corresponding author: Tao Deng,** School of Electronic and Information Engineering, Beijing Jiaotong University, Beijing 100044, P.R. China, e-mail: dengtao@bjtu.edu.cn
Shasha Li, Yang Zhang, Yuning Li and Weijie Yin: School of Electronic and Information Engineering, Beijing Jiaotong University, Beijing 100044, P.R. China. https://orcid.org/0000-0001-6957-5003 (S. Li)
Qi Chen and Zewen Liu: Institute of Microelectronics, Tsinghua University, Beijing 100084, P.R. China

1 Introduction

Ultraviolet (UV) photodetectors are important for many applications such as space communication, flame detection, military surveillance, industrial quality control, and environmental monitoring [1–10]. Due to the excellent electrical and optical properties, such as ultrafast carrier mobility [11–12], high conductivity, ultra-wide spectral range (from UV to terahertz) [13–15] and tunable optical properties via electrostatic doping [16, 17], graphene has attracted enormous attention as a promising candidate for high-performance photodetectors. Especially, the pronounced photon absorption near the saddle-point singularity makes graphene well suited for UV photodetectors [18]. However, the photoresponsivity of pure graphene-based photodetectors is still limited within $1–2\times10^{-2}$ A W^{-1} [19–21], owing to the intrinsic low optical absorption and short minority carrier lifetime of graphene [22].

A feasible way to increase the photoresponsivity of graphene-based photodetectors is to construct Schottky-diode-like graphene-semiconductor heterojunctions [23–27]. Using a graphene-silicon heterojunction device, a photoresponsivity about 0.1 A/W was obtained in the UV region [23]. By spin-coating a layer of titanium dioxide (TiO_2) nanoparticles (NPs, size, 3–5 nm) [24] or Ag NPs [25] on such devices for UV light absorption, the photoresponsivity could be further increased by up to ~100%. To further increase the photoresponsivity of graphene-based UV photodetectors, graphene membranes were integrated with various semiconducting light harvesters, such as transition-metal dichalcogenides [28, 29], fullerene (C_{60}) [30], organic molecules [31], and quantum-dots (QDs) [32, 33], based on the photogating effect. For example by synthesizing a layer of silicon QDs doped with boron on a back-gated graphene field-effect transistor (GFET), a photoresponsivity up to ~10^8 A/W and a detectivity of ~10^{12} Jones were obtained at 375 nm [33]. However, as most of the existing light harvesters have modest bandgaps, the corresponding graphene UV photodetectors are not

solar-blind, limiting their applications to some military and civilian fields such as missile interception, biological analysis, and UV radiation monitoring below the ozone hole [26]. Furthermore, the synthesis techniques of some light harvesters and the processes of integrating them with graphene are complex and require special equipment, leading to high cost and unavailability. Therefore, sensitive, solar-blind, and cost-effective UV photodetectors are still highly desirable.

In this paper, a simple and feasible technique was demonstrated to realize highly sensitive and solar-blind UV photodetectors, by decorating a buried-gated GFET with solution-synthesized TiO_2 NPs. The buried-gate structure allows tunable optical properties via a small gate voltage, while the solution-synthesized TiO_2 NPs, which are solar-blind, nontoxic, low-cost and long-term stable [24, 34, 35], significantly increases the photoresponsivity. Under the illumination of a 325-nm laser with an intensity of 11 W/cm^2, a photoresponsivity of 118.3 A/W and a detectivity of 1.75×10^{11} Jones were obtained, at the conditions of zero gate bias and a source-drain bias voltage of 0.2 V. Furthermore, the photoresponsivity and photoresponse time of the devices can be easily modulated by applying a small (≤1 V) gate bias or/and changing the source-drain bias voltages, to meet the needs in different application situations.

2 Experiments

The buried-gate GFETs were fabricated using a similar method shown in our previous work [36]. The buried chromium (Cr)/gold (Au) gate electrodes with thicknesses of 10 and 30 nm were deposited on a substrate consisted of 200-nm-thick silicon nitride (Si_3N_4), 50-nm-thick aluminum (Al), and 500-μm-thick silicon (Si), using magnetron sputtering. Next, a layer of silicon dioxide (SiO_2) with the thickness of 30 nm was deposited by plasma-enhanced chemical vapor deposition, to form the dielectric layer. Then, monolayer graphene (ACS Material, LLC) was transferred onto the SiO_2 layer and patterned using oxygen plasma etching. After this step, Cr/Au (10 nm/50 nm) source and drain electrodes were deposited on the graphene layer by electron beam evaporation and the buried-gate GFETs were obtained (Figure 1A).

The TiO_2 NPs were synthesized using the sol-gel method [24]. Firstly, a mixed solution of $TiCl_4$ (1 ml), ethanol (5 ml), and benzyl alcohol (35 ml) with a volume ratio of 2.4:12.2:85.4 was heated at 80°C for 6 h. The $TiCl_4$, ethanol and benzyl alcohol were purchased from Sinopharm Chemical Reagent Co., Ltd., Shanghai, China. Then, the product was washed three times with diethyl ether (Sinopharm Chemical Reagent Co., Ltd., Shanghai, China) and followed by centrifugation at 12000 rpm (9200 *g*). for 10 min, to obtain the white TiO_2 precipitate. Finally, the TiO_2 precipitate was dispersed in ethanol to obtain an ethanol suspension of TiO_2 NPs with a mass concentration of 4 mg/ml. The average diameter of the TiO_2 NPs synthesized using this method is about 3–5 nm [24]. By dropping the suspension of TiO_2 NPs (4 mg/ml) onto the surface of graphene of the buried-gate GFETs, and drying them in the air, TiO_2 NPs decorated GFETs were obtained (Figure 1B).

Scanning electron microscopy (SEM) and atomic force microscopy (AFM) measurements were carried out to characterize the morphological and structural properties of the buried-gate GFETs before and after the TiO_2 NPs decoration process. Raman spectroscopy and energy dispersive X-ray spectroscopy (EDS) were also performed to analyze the components of the devices. The electrical properties of the buried-gate GFETs with and without TiO_2 NPs were investigated using a semiconductor parameter analyzer (B1500A, Keysight) and a probe station (Summit 12000, Cascade) at room temperature.

In order to investigate the photoelectrical properties of the TiO_2 NPs decorated GFETs, the wafer was diced into small (5 mm × 5 mm) chips, and bonded onto printed circuit boards with Au wires. In the photoelectrical experiments, a 325-nm laser beam with a spot size of ~2 μm, which was generated by a laser confocal Raman spectrometer (LabRam HR-800, Horiba JobinYvon), was illuminated to the conductive channel of the TiO_2 NPs decorated GFETs. A precision source/measure unit (B2911A, Agilent) was used to supply the source-drain bias voltage and monitor the source-drain current of the GFETs, while a source-meter (2400, Keithley) was used to supply the gate bias. All photoelectrical measurements were performed at room temperature and under ambient conditions.

3 Results and discussion

The schematics of buried-gate GFETs before and after the decoration of TiO_2 NPs are shown in Figure 1A,B, respectively. The dimension (length × width) of the graphene conductive channel is 30 μm × 200 μm, while the lengths of the source, drain, and gate electrodes and the intervals between them are 10 μm. Figure 1C shows a SEM micro-image of a 2 × 5 array of TiO_2 NPs decorated GFETs,

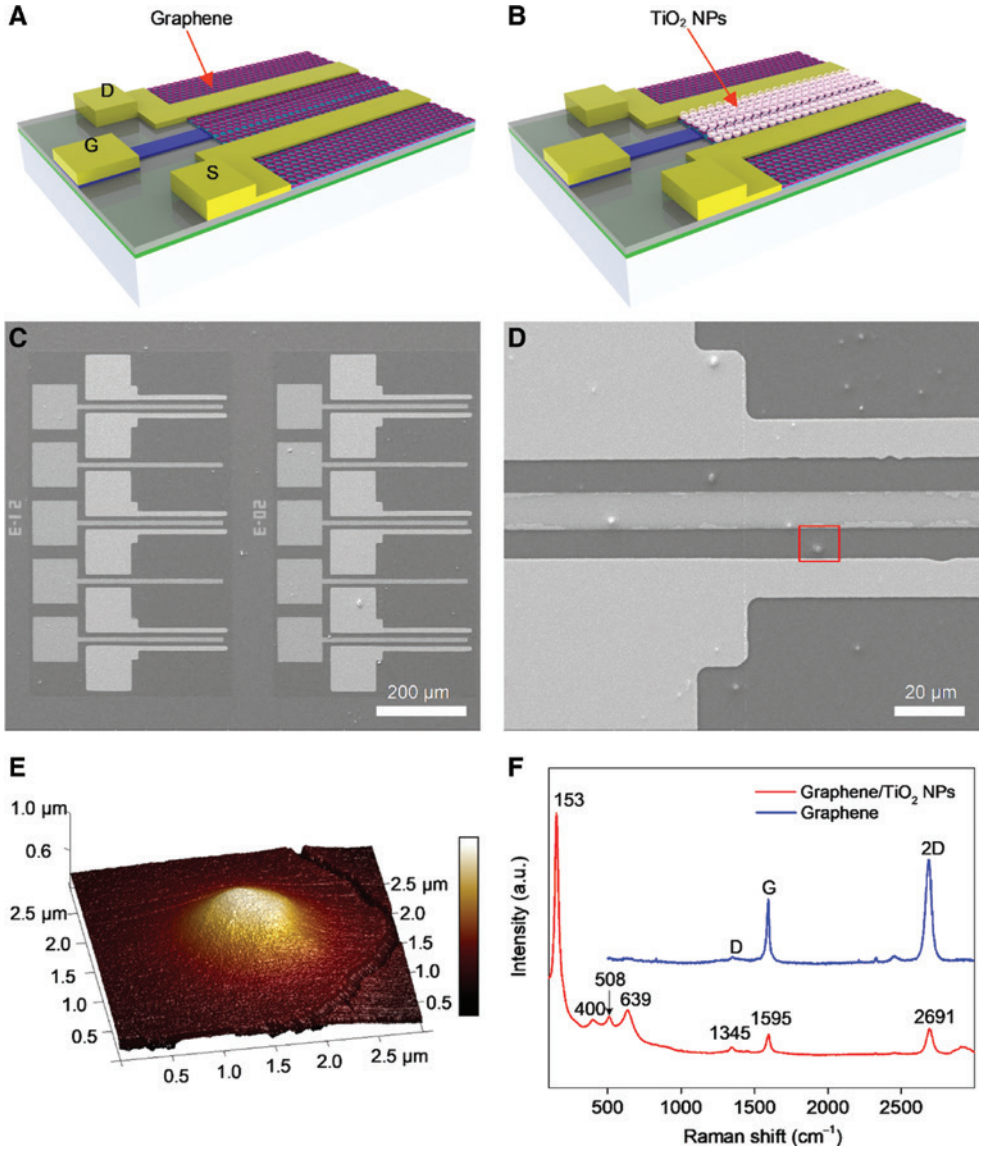

Figure 1: Titanium dioxide (TiO_2) nanoparticles (NPs) decorated buried-gate graphene field-effect transistors (GFETs). (A) and (B) Buried-gate GFETs before and after the decoration of TiO_2 NPs on the surface of graphene. (C) Scanning electron microscopy micro-image of a 2×5 array of TiO_2 NPs decorated GFETs. (D) Zoomed-in details of the graphene/TiO_2 NPs conductive channel. (E) Atomic force microscopy micro-image of agglomerated TiO_2 NPs (marked in red box in Figure 1D). (F) Typical Raman spectra of the GFETs with (red line) and without (blue line) TiO_2 NPs.

indicating the potential for large-scale integration of the devices, which is important in sensing and imaging areas [13, 30, 37]. From the zoomed-in SEM micro-image of a TiO_2 NPs decorated GFET (Figure 1D), the source, drain, and gate electrodes are well constructed, and the conductive channel is relatively smooth, except for several agglomerates. An EDS measurement was performed on one of the agglomerates in the center of the conductive channel (labeled by red box in Figure 1D). Significant Ti and O peaks were observed in the EDS spectroscopy (Figure S1C), indicating the agglomerates consisted of TiO_2 NPs. More EDS measurements were carried out at different positions in the conductive channel, and demonstrated that the whole channel was coated with a thin layer of TiO_2 NPs (Figure S1C–S1F).

Atomic force microscopy measurements were also performed to characterize the morphology of the TiO_2 NPs decorated graphene conductive channel, as shown in Figure 1E. It can be seen that the bottom diameter of the TiO_2 NPs agglomerate is about 2 μm and the height is about 1 μm. The average thickness of the TiO_2 NP layer far away from the agglomerate is less than 500 nm. According

to the work reported by Zhu et al. [24], the optimal thickness of the TiO_2 NP layer for UV light harvesting is between 250 and 500 nm, and the agglomerates of TiO_2 NPs will decrease the UV light harvesting efficiency. Therefore, the TiO_2 NPs decoration process should be optimized carefully. We further characterized the buried-gate GFETs with and without TiO_2 NPs using the Raman spectroscopy and confirmed the presence of both graphene and TiO_2 in the TiO_2 NPs decorated GFETs (Figure 1F). For the buried-gate GFETs without TiO_2 NPs, the characteristic G and 2D peaks of graphene locate at 1594 and 2686 cm^{-1}, respectively. After the decoration of TiO_2 NPs, both G and 2D peaks of graphene are slightly up-shifted, 1 cm^{-1} for the G peak and 5 cm^{-1} for the 2D peak. Simultaneously, the characteristic TiO_2 peaks are observed at 153, 400, 508, and 640 cm^{-1} [38, 39], in the TiO_2 NPs decorated GFETs.

Figure 2A shows the transfer curves of the buried-gate GFETs before and after the TiO_2 NPs decoration. A typical ambipolar characteristic can be clearly observed in the GFET without TiO_2 NPs, where the Dirac point, which is defined as the gate voltage (V_{gs}) at minimum conductance, locates at 9.8 V, indicating the graphene is p-type doped by H_2O, O_2, or other contaminations [40, 41]. After the TiO_2 NPs decoration, no Dirac point is observed within the gate voltage range from –2 to 20 V, and the source-drain current decreases monotonously with the increase of gate voltage. It is worth noting that the slope of the transfer curve of the GFET with TiO_2 NPs is smaller than that of the GFET without TiO_2 NPs in the p-type linear region. The source-drain current (I_{ds}) of the former is also smaller than that of the latter, under the same gate voltages, indicating the conductivity of the graphene degrades in the TiO_2 NPs decoration process. These phenomena were opposite with the observation reported by Zheng et al. [35], and need to be carefully investigated in the future. From the enlarged transfer characteristic curve of the TiO_2 NPs decorated GFET (Figure 2B), the gate modulation effect still exists, although it is weaker than that of the GFET without TiO_2 NPs. In order to investigate the effect of TiO_2 NPs on the carrier mobility (μ) and contact resistance ($R_{contact}$) of the device, a model proposed by Kim et al. [42] was used to analyze the resistive behavior of the devices. Detailed information about the analysis can be found in Figure S2. For the GFET without TiO_2 NPs, $\mu = 764$ $cm^2/(V\ s)$, and $R_{contact} = 147\ \Omega$. After coating TiO_2 NPs, the carrier mobility of the GFET decreases to $\mu = 690$ $cm^2/(V\ s)$, and the contact resistance increases to $R_{contact} = 405\ \Omega$. These phenomena can be attributed to increased disorder caused by

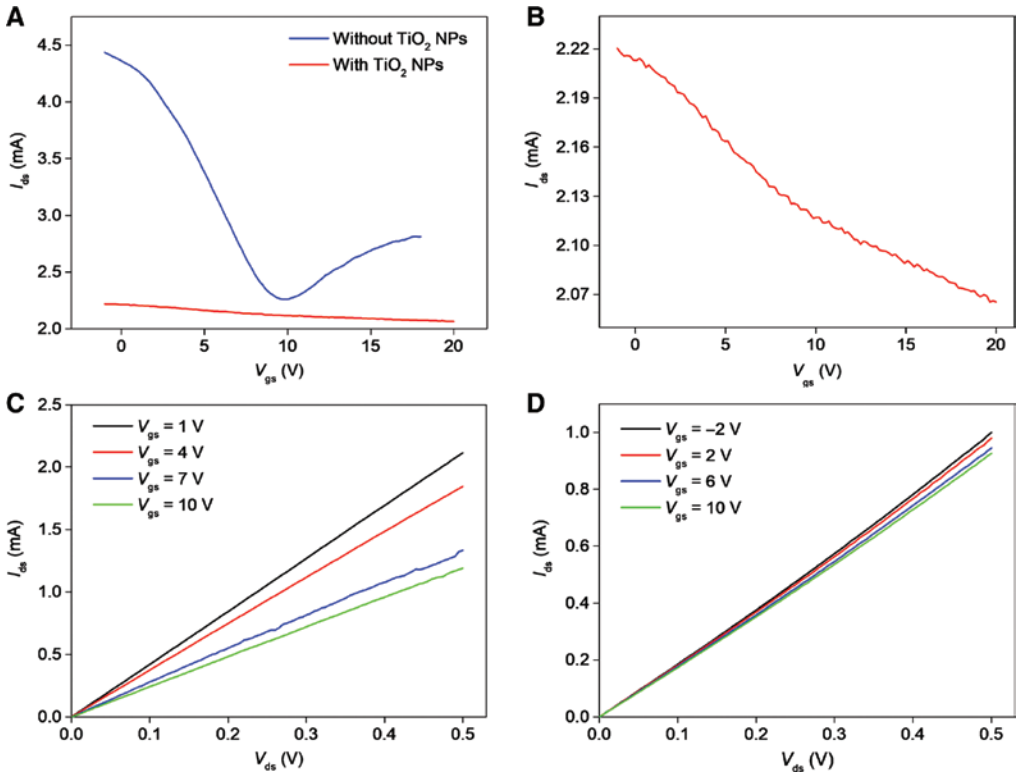

Figure 2: Electrical properties of the GFETs before and after the TiO_2 NPs decoration process.
(A) Comparison of the transfer characteristics for GFETs with (red curve) and without (blue curve) TiO_2 NPs. (B) The transfer characteristic of the TiO_2 NPs decorated GFET. (C) and (D) Output characteristics of the GFETs without and with TiO_2 NPs, respectively.

perturbations to the graphene surface during the coating process [43, 44]. Figure 2C,D display the output characteristics of the buried-gate GFETs without and with TiO_2 NPs, respectively. Under a certain gate voltage, the source-drain current of the GFET without TiO_2 NPs increases linearly with the increase of the gate voltage (Figure 2C). Similar phenomenon is also observed in the GFET with TiO_2 NPs (Figure 2D). The source-drain current of the GFETs with and without TiO_2 NPs also changes with the gate voltage, indicating reliable gate modulation capability.

The photoelectrical properties of the buried-gate GFETs with and without TiO_2 NPs decoration were characterized using an experimental setup shown in Figure 3A. Figure 3B shows the on/off source-drain current (I_{ds}) of the TiO_2 NPs decorated GFET under the illumination of a 325-nm laser with a power of 3.47 mW, at the conditions of zero gate bias (V_{gs}) and a source-drain bias voltage (V_{ds}) of 0.1 V. As mentioned above, the Dirac point of the TiO_2 NPs decorated GFET is over than 20 V (Figure 2B), the carrier transport in the graphene channel of the TiO_2 NPs decorated GFET under zero gate bias is hole-dominant. When the TiO_2 NPs decorated GFET is exposed to UV light, the ground-state electrons in TiO_2 NPs are activated into the excited state, producing a large amount of free electrons which are injected into the graphene layer (see the inset of Figure 3C). The photogenerated electrons from TiO_2 NPs and photogating-induced electrons recombine with the dominant holes in the graphene channel, leading to a decreased conductivity. Thus, the I_{ds} decreases immediately and significantly when the laser is turned on. Once the laser is turned off, the photogenerated electrons and holes in the TiO_2 NPs recombine with each other, resulting in that the density of the dominant holes in the graphene channel recovers to its original level, so does the I_{ds}. After several on-off cycles, the photocurrent, which is defined as the difference between the source-drain current under UV light illumination and the dark source-drain current, is well retained, demonstrating good reliability and reversibility

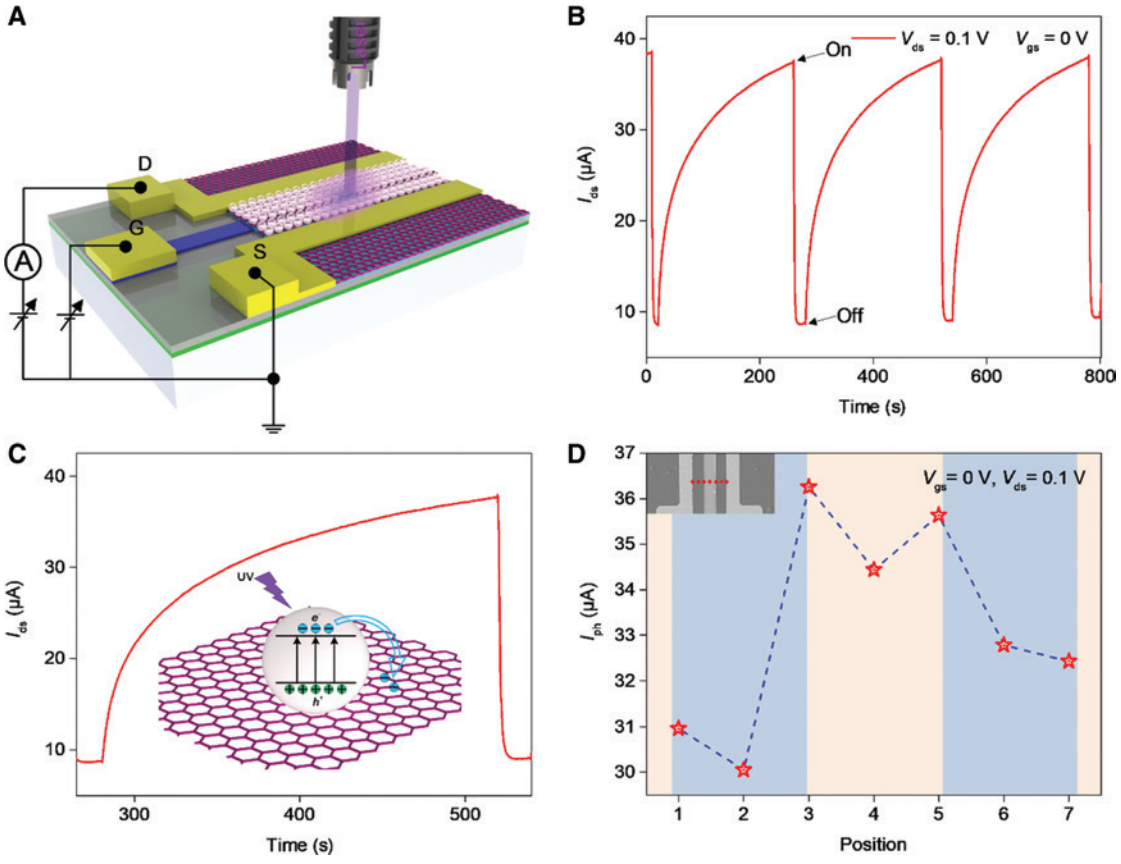

Figure 3: Photoresponse of the TiO_2 NPs decorated GFETs.
(A) Schematic of the experimental setup. (B) Temporal photocurrent response of the TiO_2 NPs decorated GFETs, under zero gate bias (V_{gs}) and a source-drain voltage (V_{ds}) of 0.1 V. (C) A single modulation cycle of temporal photocurrent response for the TiO_2 NPs decorated GFET. The inset illustrates the operation mechanism of the device. (D) The laser position dependence of the photocurrent, under the conditions of V_{gs} = 0 V and V_{ds} = 0.1 V. Inset: SEM micro-image of the device with 7 laser positions. A 325-nm laser was used in the experiments, the laser powers for (B) and (C) were 3.47 mW, while that for (D) was 1.74 mW.

of the devices. It is worth noting that there was no significant photocurrent observed under the 514-nm laser illumination (Figure S3), at the same conditions. These results indicate that the TiO_2 NPs decorated GFET photodetector is solar-blind.

To investigate the photoresponse speed of the TiO_2 NPs decorated GFET photodetectors, the rise/decay time is defined as the photocurrent increases/decreases from 10/90% to 90/10% of the stable photocurrent. From a zoomed-in single modulation cycle (Figure 3C), the rise time and the decay time are extracted to be 2.0 and 158.7 s, respectively. The photoresponse speed of the TiO_2 NPs decorated GFET photodetector is relatively slow, which can be attributed to the long-lived charge trapping achieved by the spatial separation of photoexcited charges across the graphene/TiO_2 interface [35, 39]. The lifetime of the trapped charges in the semiconductor light harvesters is influenced by many factors, such as defect types, trap-state density, and defect trap depths [45]. By varying the above factors, the charge trap lifetime can be significantly reduced [33]. Furthermore, the photoresponse speed of the TiO_2 NPs decorated GFET photodetector can also be tuned by the source-drain bias and gate bias, which will be discussed below.

Thanks to the small spot size of the laser (~2 μm), scanning photocurrent experiments were performed by mechanically moving the TiO_2 NPs decorated GFET photodetector step by step to change the laser beam position between the source and drain electrodes, as illustrated in the inset of Figure 3D. The experimental result (Figure 3D) demonstrates that photocurrent generation clearly arises from the graphene/TiO_2 NPs hybrid channel rather than electrode/channel junctions or other regions, indicating the photogating effect dominates the photoresponse [46]. More experiments found that the laser position on the TiO_2/graphene channel of the device affects not only the photocurrent but also the photoresponse speed, as shown in Figure S4. In the following experiments, the laser position was fixed in the middle of the channel.

Figure 4A shows temporal photoresponses of the TiO_2 NPs decorated GFET under different source-drain

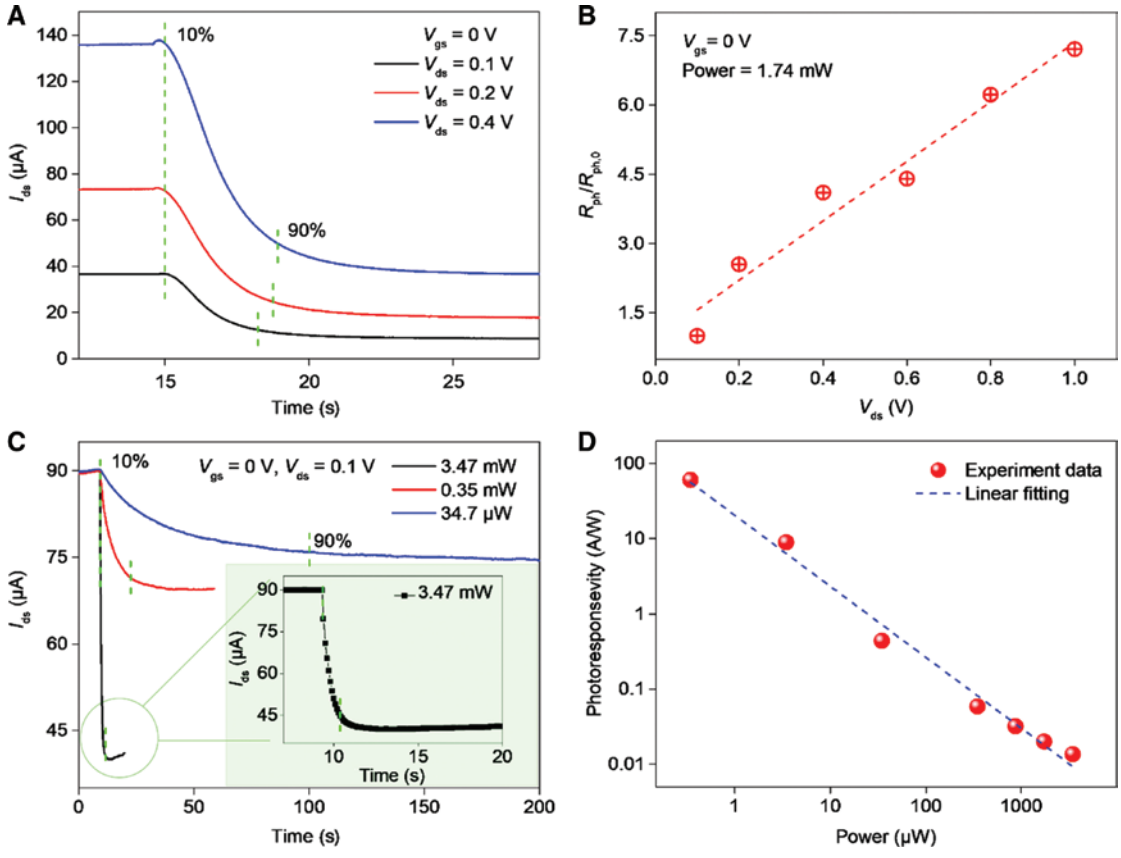

Figure 4: Photoelectrical properties of the TiO_2 NPs decorated GFET photodetectors.
(A) Photoresponses at different source-drain bias voltages (V_{ds}), under the conditions of zero gate bias (V_{gs} = 0 V) and an incident laser power of 1.74 mW. (B) The normalized photoresponsivity [$R_{ph}/R_{ph,0}$, where $R_{ph,0}$ is the photoresponsivity (R_{ph}) obtained at V_{ds} = 0.1 V] as a function of the V_{ds}, under the conditions of an incident laser power of 1.74 mW and V_{gs} = 0 V. (C) Photoresponses under different incident laser powers. (D) The photoresponsivity as a function of incident laser power, at V_{ds} = 0.1 and V_{gs} = 0 V.

bias voltages (V_{ds}), at the conditions of an incident laser power of 1.74 mW (325 nm) and zero gate bias ($V_{gs} = 0$ V). With the increase of the V_{ds}, the photocurrent increases, as well as the dark current. Furthermore, the rise times (τ_{on}) of the photoresponses under different source-drain bias voltages of 0.1, 0.2, and 0.4 V are 3.23, 3.75, and 3.91 s, respectively. This result indicates that the photoresponse speed becomes slower with the increase of the source-drain bias voltage. The photoresponsivity (R_{ph}) is defined as $R_{ph} = I_{ph}/P$, where P is total power of the incident laser. More experiments showed that the R_{ph} increases almost linearly with the V_{ds}, as shown in Figure 4B. When the V_{ds} increases from 0.1 to 1 V, the R_{ph} increases 7.2 times. Liu and Kar [47] and Liu et al. [48] also observed similar phenomena of the linear bias voltage dependence of photoresponsivity. The photoconductive gain can be calculated by using τ/t_{tr}, where τ is the lifetime of the trapped charges, and t_{tr} is the time for the transfer of carriers through the device channel [49]. As $t_{tr} = L^2/(\mu V_{ds})$, where L is the length of the device channel and μ is the carrier mobility, the photoconductive gain is proportional to V_{ds}. The tunable photoresponsivity of photodetectors is important in some practical applications such as imaging for variable light intensity.

The photoresponses of the TiO_2 NPs decorated GFET under different incident laser powers are plotted in Figure 4C. The source-drain bias voltage is 0.1 V, while the gate bias voltage is 0 V. It can be seen that the photocurrent rises with the increase of the incident laser power. Furthermore, the rise times (τ_{on}) of the photoresponses under different laser powers of 3.47 mW, 0.35 mW, and 34.7 μW are 1.1, 12.7, and 91.4 s, respectively, as shown in Table 1, indicating that higher laser power results in faster photoresponse speed. This phenomenon was also observed by Tan et al. in a black phosphorus carbide phototransistor based on the photogating effect [50].

Figure 4D shows the photoresponsivity of the TiO_2 NPs decorated GFET photodetector as a function of the incident laser power, under the conditions of zero gate bias and a source-drain bias of 0.1 V. As with most graphene-based phototransistors based on the photogating effect [47, 48], the photoresponsivity decreases at high incident photon densities due to the saturated absorption and the weakened built-in field [32]. A photoresponsivity as high as 60.3 A/W was obtained under the laser power of 0.35 μW (11.1 W/cm^2). It is worth noting that the laser power mentioned here is the total incident laser power, rather than the laser power on the graphene conductive channel. By simply increasing the source-drain bias voltage from 0.1 to 0.2 V, the photoresponsivity of the TiO_2 NPs decorated GFET can be increased to 118.3 A/W (Figure S5), which is much higher than that of the GFET before coating TiO_2 NPs (0.78 μA/W, as shown in Figure S6). Furthermore, this photoresponsivity (118.3 A/W) is over 600 times higher than that of a recently reported solar-blind UV photodetector based on graphene/vertical Ga_2O_3 nanowire array heterojunction (0.185 A/W) [26]. We would like to point that the photoresponse time of our device now is in the level of several seconds to hundreds of seconds, which is much slower than that of the graphene/Ga_2O_3 photodetector (~8 ms) [26]. A major reason is that the graphene/Ga_2O_3 photodetector is a photodiode, while our device is a phototransistor. The typical photoresponse time of graphene-based phototransistors is in the level of several seconds, such as the Si quantum dot/graphene phototransistors reported by Ni et al. [33] and the graphene/MoS_2 phototransistors reported by Roy et al. [51]. Other reasons for the slow photoresponse of our device are related to the photosensitive materials and their morphologies. For example, there are a lot of trap states in TiO_2 NPs and the graphene/TiO_2 interface, which trap photogenerated electrons, resulting in a slow photoresponse [24]. In order to improve the photoresponse speed of the TiO_2 NPs decorated GFET photodetectors, gate pulses [52] may be employed to sweep out the trapped carriers of TiO_2 NPs within an appropriate time frame in the future. Another important parameter of photodetector is the specific detectivity (D^*), which determines the capability of a photodetector to detect a weak light signal, can be given as $D^* = \frac{R \cdot A^{1/2}}{\sqrt{2 \cdot e \cdot I_{dark}}}$ [53], where R is photoresponsivity, A is the effective photoactive area of detector, e is the electron charge, and I_{dark} is the dark current. Using the photoresponsivity of 60.3 A/W, a $D^* = 1.24 \times 10^{11}$ jones (1 jones = 1 cm Hz$^{1/2}$ W^{-1}) is obtained, which is comparable to the best performances of reported graphene-based UV photodetectors [39, 54]. Importantly, the photoresponsivity and detectivity can be further enhanced at lower incident laser powers [27, 29, 53].

Temporal photoresponses of the TiO_2 NPs decorated GFET under different gate bias voltages are plotted in Figure 5A. The magnitudes of the photocurrents under different gate bias voltages are different, so are

Table 1: The photoresponse times of the TiO_2 nanoparticles (NPs) decorated graphene field-effect transistor (GFET) photodetector under 325-nm laser illuminations with different powers ($V_{gs} = 0$ V, $V_{ds} = 0.1$ V).

Laser power (μW)	3470	1740	870	350	34.7
Photoresponse time (s)	1.1	1.6	4.1	12.7	91.4

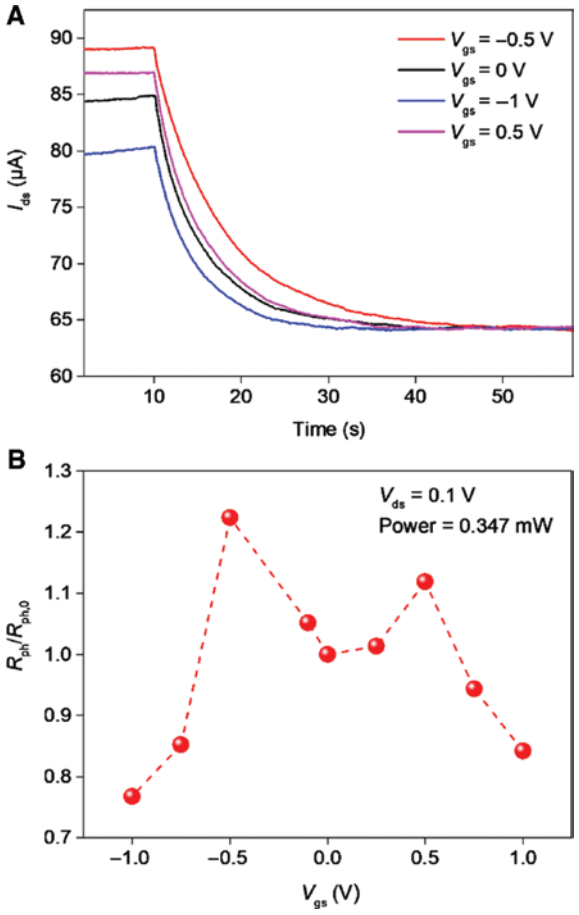

Figure 5: The gate-voltage-dependent photoresponse of the TiO_2 NPs decorated GFET photodetectors.
(A) Temporal photocurrent responses of the TiO_2 NPs decorated GFET photodetector at different gate bias voltages (V_{gs}), under the conditions of a laser power of 0.347 mW and V_{ds} = 0.1 V. (B) The gate-voltage-dependent photoresponsivity (R_{ph}) of the TiO_2 NPs decorated GFET photodetectors, where $R_{ph,0}$ is the R_{ph} at V_{ds} = 0.1 V and V_{gs} = 0 V. The incident laser power is 0.347 mW.

the photoresponse speeds. The photocurrent under V_{gs} = −0.5 V is 52.7% larger than that under V_{gs} = −1 V, while the rise time of the photoresponse under V_{gs} = −0.5 V is 65.7% slower than that under V_{gs} = −1 V. More experiments showed that the photoresposivity of the TiO_2 NPs decorated GFET can be modulated by gate bias voltages, as shown in Figure 5B. With the increase of the gate voltage from 0 to 1 V, the photoresponsivity increases first and then decreases the threshold gate voltage which is about 0.5 V. Similar characteristic is also observed in the negative gate voltage range. By applying a −0.5 V voltage to the buried-gate electrode, the photoresponsivity can be increased by ~20%. These results indicate both the photoresponsivity and the photoresponse speed can be modulated by the gate bias. Table 2 summarizes the reported high-performance UV photodetectors based on graphene. Obviously, the device in this work has extremely high photoresponsivity under small bias voltages, but the photoresponse speed needs to improve in the future.

4 Conclusions

A highly sensitive, solar-blind, and cost-effective UV photodetector based on a buried-gate GFET decorated with TiO_2 NPs was demonstrated in this paper. The TiO_2 NPs significantly enhance the UV light absorption of the device. Under the illumination of a 325-nm laser with an incident power of 0.35 μW, a photoresponsivity as high as 118.3 A/W and a detectivity of ~10^{11} Jones were obtained, at zero gate bias and a source-drain bias voltage of 0.2 V. Importantly, the photoresponsivity can

Table 2: Photoelectrical characteristics of typical ultraviolet (UV) photodetectors based on graphene.

Ref	Description	Wavelength	Responsivity	Detectivity (Jones)	Rise time
[26]	Graphene/vertical Ga_2O_3 nanowire array heterojunction	254 nm 258 nm	0.185 A/W@−5 V	–	9 ms (254 nm)
[39]	Graphene/TiO_2 nanotube heterojunction	365 nm	~20 A/W@5 V	1.9×10^{12}	>15 s
[34]	Graphene/anatase-nanosheets Schottky junction	254, 302, 365 nm	0.5 A/W@−5 V	–	140 ms (254 nm) 220 ms (302 nm)
[54]	Graphene-TiO_2 nanotube arrays heterojunction	365 nm	0.126 A/W@−0.5 V	3.3×10^{11}	–
[55]	3D tubular GFETs	UV, visible, MIR, THz	1 A/W@0 V(UV)	–	265 ns
[56]	Graphene/β-Ga_2O_3 heterojunction	254 nm	12.8 A/W@−6 V	1.3×10^{13}	1.5 ms
[25]	Ag NPs enhanced graphene/GaAs heterojunction	325–980 nm	0.186 A/W@0 V (325 nm)	2.63×10^{13} (325 nm)	–
[27]	Graphene β-Ga_2O_3 heterojunction	254 nm	39.3 A/W@20 V	5.92×10^{13}	94.83 s@4 V
[57]	Graphene/n-type SiC Schottky	325 nm	2.18 A/W@−5 V	–	>0.39 s and <4.46 s
This work	TiO_2 NPs decorated GFETs	325 nm	118.3 A/W@0.2 V	1.75×10^{11}	>1.1 s

be further enhanced by increasing the source-drain bias voltage or properly tuning the gate bias voltage. Furthermore, the photoresponse speed of the TiO_2 NPs decorated GFET photodetectors can also be tuned by the source-drain bias and gate bias.

Supplementary material: See Supplementary material for energy X-ray spectrum of the buried-gate TiO_2 NPs GFETs, the carrier mobility and graphene-metal contact resistance of the buried-gate GFET with and without TiO_2 NPs, the photoresponse of the device under the 514 nm illumination, the influence of the incident laser position on photoresponse time, the photoresponsivity of the device before coating TiO_2 NPs, and the temporal photoresponse of the buried-gate TiO_2 NPs GFET at $V_{ds} = 0.2$ V.

Acknowledgments: This research was supported by the National Natural Science Foundation of China (61604009), the Fundamental Research Funds for the Central Universities (2018JBM002), and the Beijing Municipal Natural Science Foundation (4164095).

References

[1] Zhang H, Babichev AV, Jacopin G, et al. Characterization and modeling of a ZnO nanowire ultraviolet photodetector with graphene transparent contact. J Appl Phys 2013;114:234505.
[2] Chen CS, Zhou P, Wang N, Ma Y, San HS. UV-assisted photochemical synthesis of reduced graphene oxide/ZnO nanowires composite for photoresponse enhancement in UV photodetectors. Nanomaterials 2018;8:26.
[3] Hajimazdarani M, Naderi N, Yarmand B, Kolahi A, Sangpour P. Enhanced optical properties of ZnS-rGO nanocomposites for ultraviolet detection applications. Ceramics Int 2018;44:17878–84.
[4] Chava VSN, Omar SU, Brown G, et al. Evidence of minority carrier injection efficiency >90% in an epitaxial graphene/SiC Schottky emitter bipolar junction phototransistor for ultraviolet detection. Appl Phys Lett 2016;108:043502.
[5] Tsukazaki A, Ohtomo A, Onuma T, et al. Repeated temperature modulation epitaxy for p-type doping and light-emitting diode based on ZnO. Nat Mater 2005;4:42–6.
[6] Wan Q, Li QH, Chen YJ, et al. Fabrication and ethanol sensing characteristics of ZnO nanowire gas sensors. Appl Phys Lett 2004;84:3654.
[7] Law M, Greene LE, Johnson JC, Saykally R, Yang PD. Nanowire dye-sensitized solar cells. Nat Mater 2005;4:455–9.
[8] Wang ZL, Song JH. Piezoelectric nanogenerators based on zinc oxide nanowire arrays. Science 2006;312:242–6.
[9] Prakash N, Singh M, Kumar G, et al. Ultrasensitive self-powered large area planar GaN UV-photodetector using reduced graphene oxide electrodes. Appl Phys Lett 2016;109:242102.
[10] Arora K, Goel N, Kumar M, Kumar M. Ultrahigh performance of self-powered β-Ga_2O_3 thin film solar-blind photodetector grown on cost-effective Si substrate using high-temperature seed layer. ACS Photonics 2018;5:2391–401.
[11] Dawlaty JM, Shivaraman S, Chandrashekhar M, Rana F, Spencer MG. Measurement of ultrafast carrier dynamics in epitaxial graphene. Appl Phys Lett 2008;92:042116.
[12] Brida D, Tomadin A, Manzoni C, et al. Ultrafast collinear scattering and carrier multiplication in graphene. Nat Commun 2013;4:1987.
[13] Koppens FHL, Mueller T, Avouris P, Ferrari AC, Vitiello MS, Polini M. Photodetectors based on graphene, other two-dimensional materials and hybrid systems. Nat Nanotechnol 2014;9:780–93.
[14] Long MS, Wang P, Fang HH, Hu WD. Progress, challenges, and opportunities for 2D material based photodetectors. Adv Funct Mater 2018;1803807.
[15] Liu N, Tian H, Schwartz G, Tok JBH, Ren TL, Bao ZN. Large-area, transparent, and flexible infrared photodetector fabricated using P-N junctions formed by N-doping chemical vapor deposition grown graphene. Nano Lett 2014;14:3702–8.
[16] Li ZQ, Henriksen EA, Jiang Z, et al. Dirac charge dynamics in graphene by infrared spectroscopy. Nat Phys 2008;4:532–5.
[17] Wang F, Zhang YB, Tian CS, et al. Gate-variable optical transitions in graphene. Science 2008;320:206–9.
[18] Mak KF, Shan J, Heinz TF. Seeing many-body effects in single- and few-layer graphene: observation of two-dimensional saddle-point excitons. Phys Rev Lett 2011;106:046401.
[19] Echtermeyer TJ, Britnell L, Jasnos PK, et al. Strong plasmonic enhancement of photovoltage in graphene. Nat Commun 2011;2:458.
[20] Engel M, Steiner M, Lombardo A, et al. Light-matter interaction in a microcavity-controlled graphene transistor. Nat Commun 2012;3:906.
[21] Furchi M, Urich A, Pospischil A, et al. Microcavity-integrated graphene photodetector. Nano Lett 2012;12:2773–7.
[22] Breusing M, Ropers C, Elsaesser T. Ultrafast carrier dynamics in graphite. Phys Rev Lett 2009;102:086809.
[23] An XH, Liu FZ, Jung YJ, Kar S. Tunable graphene-silicon heterojunctions for ultrasensitive photodetection. Nano Lett 2013;13:909–16.
[24] Zhu M, Zhang L, Li XM, et al. TiO_2 enhanced ultraviolet detection based on a graphene/Si Schottky diode. J Mater Chem A 2015;3:8133–8.
[25] Lu YH, Feng SR, Wu ZQ, et al. Broadband surface plasmon resonance enhanced self-powered graphene/GaAs photodetector with ultrahigh detectivity. Nano Energy 2018;47:140–9.
[26] He T, Zhao YK, Zhang XD, et al. Solar-blind ultraviolet photodetector based on graphene/vertical Ga_2O_3 nanowire array heterojunction. Nanophotonics 2018;7:1557–62.
[27] Kong WY, Wu GA, Wang KY, et al. Graphene-β-Ga_2O_3heterojunction for highly sensitive deep UV photodetector application. Adv Mater 2016;28:10725–31.
[28] Mehew JD, Unal S, Alonso ET, et al. Fast and highly sensitive ionic-polymer-gated WS_2-graphene photodetectors. Adv Mater 2017;29:1700222.
[29] Iqbal MZ, Khan S, Siddique S. Ultraviolet-light-driven photoresponse of chemical vapor deposition grown molybdenum disulfide/graphene heterostructured FET. Appl Surf Sci 2018;459:853–9.
[30] Qin SC, Chen XQ, Du QQ, et al. Sensitive and robust ultraviolet photodetector array based on self-assembled graphene/C_{60} hybrid films. ACS Appl Mater Interfaces 2018;10:38326–33.

[31] Liu XL, Luo XG, Nan HY, et al. Epitaxial ultrathin organic crystals on graphene for high efficiency phototransistors. Adv Mater 2016;28:5200–5.
[32] Konstantatos G, Badioli M, Gaudreau L, et al. Hybrid graphene-quantum dot phototransistors with ultrahigh gain. Nat Nanotechnol 2012;7:363–8.
[33] Ni ZY, Ma LL, Du SC, et al. Plasmonic silicon quantum dots enabled high-sensitivity ultra-broadband photodetection of graphene-based hybrid phototransistors. ACS Nano 2017;11:9854–62.
[34] Liu Y, Cai HL, Wang FF, et al. Graphene on {116} faceted monocrystalline anatase nanosheet array for ultraviolet detection. Nanoscale 2018;10:3606–12.
[35] Zheng KH, Meng FB, Jiang L, Yan QY, Hng HH, Chen XD. Visible photoresponse of single-layer graphene decorated with TiO_2 nanoparticles. Small 2013;9:2076–80.
[36] Su F, Zhang ZH, Li SS, Li PA, Deng T. Long-term stability of photodetectors based on graphene field-effect transistors encapsulated with Si_3N_4 layers. Appl Surf Sci 2018;459:164–70.
[37] Tian H, Yang Y, Xie D, et al. Wafer-scale integration of graphene-based electronic, optoelectronic and electroacoustic devices. Sci Rep 2014;4:3598.
[38] Chen DJ, Zou LL, Li SX, Zheng FY. Nanospherical like reduced graphene oxide decorated TiO_2 nanoparticles: an advanced catalyst for the hydrogen evolution reaction. Sci Rep 2016;6:20335.
[39] Noothongkaew S, Thumthan O, An KS. Minimal layer graphene/TiO_2 nanotube membranes used for enhancement of UV photodetectors. Mater Lett 2018;218:274–9.
[40] Wang ZG, Chen YF, Li PJ, et al. Effects of methane flux on structural and transport properties of CVD-grown graphene films. Vacuum 2012;86:895–8.
[41] Srivastava A, Galande C, Ci L, et al. Novel liquid precursor-based facile synthesis of large-area continuous, single, and few-layer graphene films. Chem Mater 2010;22:3457–61.
[42] Kim S, Nah J, Jo I, et al. Realization of a high mobility dual-gated graphene field-effect transistor with Al_2O_3 dielectric. Appl Phys Lett 2009;94:062107.
[43] Farmer DB, Chiu HY, Lin YM, Jenkins KA, Xia FN, Avouris P. Utilization of a buffered dielectric to achieve high field-effect carrier mobility in graphene transistors. Nano Lett 2009;9:4474–8.
[44] Ishigami M, Chen JH, Cullen WG, Fuhrer MS, Williams ED. Atomic structure of graphene on SiO_2. Nano Lett 2007;7:1643–8.
[45] Zhang YZ, Liu T, Meng B, et al. Broadband high photoresponse from pure monolayer graphene photodetector. Nat Commun 2013;4:1811.
[46] Xia FN, Mueller T, Golizadeh-Mojarad R, et al. Photocurrent imaging and efficient photon detection in a graphene transistor. Nano Lett 2009;9:1039–44.
[47] Liu FZ, Kar S. Quantum carrier reinvestment-induced ultrahigh and broadband photocurrent responses in graphene-silicon junctions. ACS Nano 2014;8:10270–9.
[48] Liu YD, Wang FQ, Wang XM, et al. Planar carbon nanotube-graphene hybrid films for high-performance broadband photodetectors. Nat Commun 2015;6:8589.
[49] Kufer D, Konstantatos G. Photo-FETs: phototransistors enabled by 2D and 0D nanomaterials. ACS Photonics 2016;3:2197–210.
[50] Tan WC, Huang L, Ng RJ, et al. A black phosphorus carbide infrared phototransistor. Adv Mater 2018;30:1705039.
[51] Roy K, Padmanabhan M, Goswami S, et al. Graphene-MoS_2 hybrid structures for multifunctional photoresponsive memory devices. Nat Nanotechnol 2013;8:826–30.
[52] Lopez-Sanchez O, Lembke D, Kayci M, Radenovic A, Kis A. Ultrasensitive photodetectors based on monolayer MoS_2. Nat Nanotechnol 2013;8:497–501.
[53] Guo N, Gong F, Liu JK, et al. Hybrid WSe_2 – In_2O_3 phototransistor with ultrahigh detectivity by efficient suppression of dark currents. ACS Appl Mater Interfaces 2017;9:34489–96.
[54] Zhang DY, Ge CW, Wang JZ, Zhang TF, Wu YC, Liang FX. Single-layer graphene-TiO_2 nanotubes array heterojunction for ultraviolet photodetector application. Appl Surf Sci 2016;387:1162–8.
[55] Deng T, Zhang ZH, Liu YX, et al. Three-dimensional graphene field-effect transistors as high-performance photodetectors. Nano Lett 2019;19:1494–503.
[56] Lin RC, Zheng W, Zhang D, et al. High-performance graphene/β-Ga_2O_3heterojunction deep-ultraviolet photodetector with hot-electron excited carrier multiplication. ACS Appl Mater Interfaces 2018;10:22419–26.
[57] Yang JW, Gou LW, Gou YL, Hu WJ, Zhang ZS. Epitaxial graphene/SiC Schottky ultraviolet photodiode with orders of magnitude adjustability in responsivity and response speed. Appl Phys Lett 2018;112:103501.

Supplementary Material: The online version of this article offers supplementary material (https://doi.org/10.1515/nanoph-2019-0060).